

High-energy gamma-ray study of the dynamically young SNR G150.3+4.5

J. Devin^{1*}, M. Lemoine-Goumard¹, M.-H. Grondin¹, D. Castro², J. Ballet³, J. Cohen² and J. W. Hewitt⁴

¹ Univ. Bordeaux, CNRS, CENBG, UMR 5797, F-33170 Gradignan, France

*e-mail: jdevin.phys@gmail.com

² Harvard-Smithsonian Center for Astrophysics, 60 Garden Street, Cambridge, MA 02138, USA

³ Laboratoire AIM, CEA-IRFU/CNRS/Université Paris Diderot, Département d'Astrophysique, CEA Saclay, 91191 Gif sur Yvette, France

⁴ University of North Florida, Department of Physics, 1 UNF Drive, Jacksonville, FL 32224, USA

Received 26 May 2020, Accepted 11 September 2020

ABSTRACT

Aims. The supernova remnant (SNR) G150.3+4.5 was recently discovered in the radio band; it exhibits a shell-like morphology with an angular size of $\sim 3^\circ$, suggesting either an old or a nearby SNR. Extended γ -ray emission spatially coincident with the SNR was reported in the *Fermi* Galactic Extended Source Catalog, with a power-law spectral index of $\Gamma = 1.91 \pm 0.09$. Studying particle acceleration in SNRs through their γ -ray emission is of primary concern to assess the nature of accelerated particles and the maximum energy they can reach.

Methods. Using more than ten years of *Fermi*-LAT data, we investigate the morphological and spectral properties of the SNR G150.3+4.5 from 300 MeV to 3 TeV. We use the latest releases of the *Fermi*-LAT catalog, the instrument response functions and the Galactic and isotropic diffuse emissions. We use ROSAT all-sky survey data to assess any thermal and nonthermal X-ray emission, and we derive minimum and maximum distance to G150.3+4.5.

Results. We describe the γ -ray emission of G150.3+4.5 by an extended component which is found to be spatially coincident with the radio SNR. The spectrum is hard and the detection of photons up to hundreds of GeV points towards an emission from a dynamically young SNR. The lack of X-ray emission gives a tight constraint on the ambient density $n_0 \leq 3.6 \times 10^{-3} \text{ cm}^{-3}$. Since G150.3+4.5 is not reported as a historical SNR, we impose a lower limit on its age of $t = 1 \text{ kyr}$. We estimate its distance to be between 0.7 and 4.5 kpc. We find that G150.3+4.5 is spectrally similar to other dynamically young and shell-type SNRs, such as RX J1713.7–3946 or Vela Junior. The broadband nonthermal emission is explained with a leptonic scenario, implying a downstream magnetic field of $B = 5 \mu\text{G}$ and acceleration of particles up to few TeV energies.

Key words. gamma rays: ISM – ISM: individual (G150.3+4.5) – ISM: supernova remnants – cosmic rays

1. Introduction

Supernova remnants (SNRs) have long been thought to be the most likely accelerators of cosmic rays (CRs) up to the knee ($\sim 3 \times 10^{15} \text{ eV}$) of the CR spectrum, with diffusive shock acceleration (DSA, Bell 1978) being the primary mechanism accelerating the charged particles to γ -ray emitting energies. The Large Area Telescope (LAT) on board the *Fermi* satellite has already demonstrated that CR protons can indeed be accelerated at SNR shocks, through detection of the characteristic “pion bump” feature due to accelerated protons colliding with ambient matter. However, evidence of CR protons is often found in some evolved SNRs interacting with molecular clouds (MCs), like IC 443 or W44 (Ackermann et al. 2013), and the maximum particle energy only reaches hundreds of GeV. Cassiopeia A, one of the youngest Galactic SNR ($t \sim 350 \text{ years}$) exhibits a γ -ray spectrum with a low-energy break (Yuan et al. 2013), characteristic of emission from CR protons, and a photon cutoff energy at a few TeV (Ahnen et al. 2017; Abeysekara et al. 2020). Thus, the question of whether SNRs can accelerate particles up to PeV energies is still open. Moreover, the spectrum of the TeV shell-like and young SNRs can often be accurately described by a leptonic scenario due to inverse Compton (IC) scattering of accelerated electrons on ambient photon fields (Acero et al. 2015).

G150.3+4.5 was first considered an SNR candidate, due to the radio detection of the brightest part of the shell, before being firmly identified as a radio SNR. Faint radio emission from the southeastern part of the shell of G150.3+4.5 (called G150.8+3.8) was first reported in Gerbrandt et al. (2014) using the Canadian Galactic Plane Survey (CGPS) and considered a strong SNR candidate due to its semi-circular shell-like appearance and its nonthermal spectrum ($\alpha = -0.62 \pm 0.07$ where $S_\nu \propto \nu^\alpha$). Using a larger extraction region ($128.2' \times 37.6'$), they derived a radio spectral index of $\alpha = -0.38 \pm 0.10$, centered on $l = 150.78^\circ$ and $b = 3.75^\circ$. Gerbrandt et al. (2014) also detected faint red optical filaments spatially coincident with the southeastern shell. Gao & Han (2014) performed follow-up observations of the region using Urumqi 6 cm survey data (as well as Effelsberg 11 cm and 21 cm data and CGPS 1420 MHz and 408 MHz observations), taking advantage of the survey’s extended Galactic latitude range, up to $b = 20^\circ$. They reported a clear detection of a 2.5° wide by 3° high ($l = 150.3^\circ$, $b = +4.5^\circ$, as illustrated in Figure 1), synchrotron emitting, shell-like object (named G150.3+4.5), bolstering an SNR origin for the radio emission. The radio spectral indices of the two brightest parts of the shell (southeastern and western sides, red boxes in Figure 1)

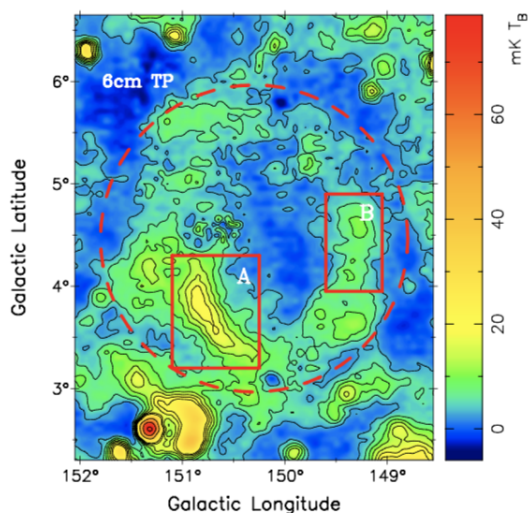


Fig. 1. Urumqi 6 cm observations of the SNR G150.3+4.5. The red boxes correspond to the brightest parts of the shell, which is represented by the red dashed circle. The figure is from Gao & Han (2014).

are $\alpha = -0.40 \pm 0.17$ and $\alpha = -0.69 \pm 0.24$ compatible with the results obtained in Gerbrandt et al. (2014).

In the Second Catalog of Hard *Fermi*-LAT Sources (2FHL, Ackermann et al. 2016), an extended source located near the radio SNR was reported (2FHL J0431.2+5553e) and modeled as a uniform disk with a radius $r = 1.27^\circ \pm 0.04^\circ$, exhibiting a hard power-law spectral index ($\Gamma = 1.7 \pm 0.2$) from 50 GeV to 2 TeV. The *Fermi* Galactic Extended Source catalog (FGES, Ackermann et al. 2017) reported a uniform disk ($r = 1.52^\circ \pm 0.03^\circ$), spatially coincident with the radio shape, but with a softer power-law spectrum ($\Gamma = 1.91 \pm 0.09$ from 10 GeV to 2 TeV) than previously derived. This FGES source is contained in the latest *Fermi*-LAT catalog (4FGL, The *Fermi*-LAT collaboration 2019), called 4FGL J0427.2+5533e, and its emission is described by a logarithmic parabola (LP) spectrum.

In this paper we present a detailed study of the γ -ray emission in the direction of G150.3+4.5 from 300 MeV to 3 TeV. In Section 2 we investigate the morphology of the γ -ray emission towards G150.3+4.5 from 1 GeV to 3 TeV and we explore its spectral properties from 300 MeV to 3 TeV. In Section 3 we use ROSAT observations to assess any thermal and nonthermal X-ray emission from the SNR, and we derive two bounding distance estimates for G150.3+4.5. Finally, in Section 4 we discuss potential γ -ray emission scenarios and model the broadband nonthermal emission from G150.3+4.5 to understand the nature of the accelerated particles.

2. *Fermi*-LAT analysis

2.1. Data reduction and preparation

The *Fermi*-LAT is a pair-conversion instrument that detects γ -ray photons in an energy range from 20 MeV to higher than hundreds of GeV (a detailed description of the instrument can be found in Atwood et al. 2009). We used ~ 10.5 years of *Fermi*-LAT data (from August 4, 2008, to January 31, 2019) and we performed a binned likelihood analysis within a region of interest (ROI) of $23^\circ \times 23^\circ$ centered on the SNR G150.3+4.5. A maximum zenith angle of 100° was applied to reduce the contamination of the Earth limb, and the time intervals during which the satellite passed through the South Atlantic Anomaly were

excluded. Since the point spread function (PSF) of the *Fermi*-LAT is energy dependent and broad at low energy, we started the morphological analysis at 1 GeV while the spectral analysis was made from 300 MeV to 3 TeV. The Summedlikelihood method was used to simultaneously fit events with different angular reconstruction quality (PSF event types). We used version 1.0.10 of the *Fermitools* and, from 1 GeV to 3 TeV, we used the *Fermipy* package (version 0.17.4, Wood et al. 2017) that allows for simultaneous morphological and spectral fits, setting a pixel size to 0.1° and eight energy bins per decade. The spectral analysis was made from 300 MeV to 3 TeV with ten energy bins per decade and a pixel size of 0.1° . For the entire analysis, we used the SOURCE event class and a preliminary inflight corrected version of the P8R3_V2 instrument response functions (IRFs) that corrects for a $\sim 10\%$ discrepancy of the PSF event type effective areas. For consistency with the 4FGL analysis, the energy dispersion was taken into account except for the isotropic diffuse emission.

To model the γ -ray data around G150.3+4.5, we started with the 4FGL catalog keeping in the model the sources located within a 20° radius from the ROI center. We used the `gll_iem_v07.fits` model to describe the Galactic diffuse emission and the isotropic templates derived using the preliminary inflight corrected version of the P8R3_V2 IRFs and extrapolated up to 3 TeV.¹ The spectral parameters of the sources in the model were first fit simultaneously with the Galactic and isotropic diffuse emissions from 1 GeV to 3 TeV. To search for additional sources in the ROI, we computed a residual test statistic (TS) map that tests in each pixel the significance of a source with a generic E^{-2} spectrum against the null hypothesis:

$$TS = 2 \times (\log \mathcal{L}_1 - \log \mathcal{L}_0). \quad (1)$$

Here \mathcal{L}_1 and \mathcal{L}_0 are the likelihood obtained with the model including and excluding the source, respectively. The TS follows a χ^2 distribution with n degrees of freedom corresponding to the additional free parameters between the models 1 and 0. We iteratively added three point sources in the model where the TS exceeded 25. We localized the position of these additional sources (RA–Dec = $52.08^\circ - 53.51^\circ$, $76.62^\circ - 45.76^\circ$ and $79.43^\circ - 50.49^\circ$) and we fit their spectral parameters simultaneously with the Galactic and isotropic diffuse emissions. The residual TS map obtained with all the sources considered in the model shows no significant residual emission, indicating that the ROI is adequately modeled.

2.2. Morphological analysis

In the 4FGL catalog, a point source (4FGL J0426.5+5434) is located in the southern part of the SNR with a significance of $\sim 25\sigma$ between 100 MeV and 1 TeV and a LP spectrum. We performed the morphological analysis from 1 GeV to 3 TeV, with the free parameters in the model being the normalization of the sources located closer than 5° from the ROI center, of the Galactic and isotropic diffuse emissions and the spectral parameters of G150.3+4.5 and 4FGL J0426.5+5434.

Using the morphological parameters of G150.3+4.5 reported in the 4FGL catalog, we first localized the position of 4FGL J0426.5+5434 and we obtained $RA_{J2000} = 66.61^\circ \pm 0.02^\circ$ and $Dec_{J2000} = 54.58^\circ \pm 0.02^\circ$ which is similar to the values reported in the 4FGL catalog ($RA_{J2000} = 66.63^\circ$ and $Dec_{J2000} =$

¹ *Fermi*-LAT background models can be found at <https://fermi.gsfc.nasa.gov/ssc/data/access/lat/BackgroundModels.html>.

	RA _{J2000} (°)	Dec _{J2000} (°)	σ or r (°)	r_{68} (°)	TS	TS _{ext}	N _{dof}
Gaussian	66.425 ± 0.060	55.371 ± 0.056	0.900 ^{+0.029} _{-0.028}	1.359 ^{+0.044} _{-0.043}	624.2	549.8	6
Disk	66.555 ± 0.172	55.314 ± 0.150	1.497 ^{+0.032} _{-0.028}	1.235 ^{+0.026} _{-0.023}	595.0	520.7	6
Urumqi 6 cm map	–	–	–	–	361.7	287.3	3

Table 1. Best-fit positions and extensions (1 GeV – 3 TeV) of G150.3+4.5 (r_{68} being the 68% containment radius) with the associated statistical errors, using a 2D symmetric Gaussian and a uniform disk model. The TS values and the number of degrees of freedom (N_{dof}) are given with respect to the null hypothesis (no emission from G150.3+4.5). The result using the Urumqi 6 cm map of the SNR, represented by the yellow contours in Figure 2, is also given.

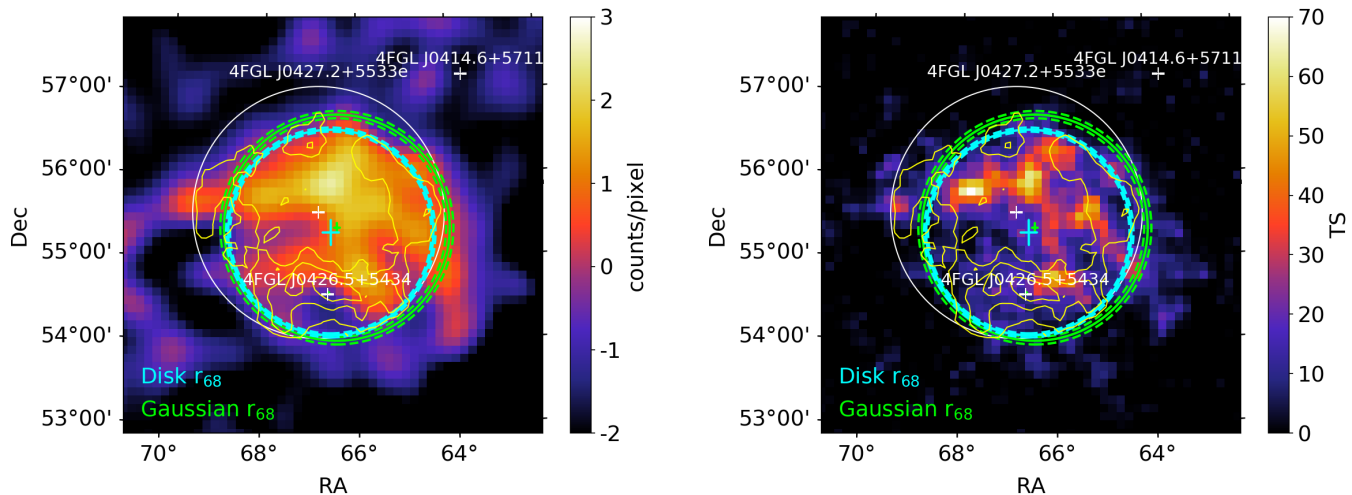


Fig. 2. Residual count map (left, smoothed with a Gaussian kernel of 0.2°) and residual TS map (right) obtained from 1 GeV to 3 TeV without G150.3+4.5 included in the model. The best-fit Gaussian and disk are represented in green and blue, respectively. The crosses are the centroid uncertainties (1σ), while the solid and dashed circles correspond to the r_{68} with its associated statistical errors (1σ). The 4FGL sources are shown in white and the Urumqi 6 cm radio contours (at 6, 11, and 16 mK T_B) are overlaid in yellow.

54.57°). We tested its extension by localizing a 2D symmetric Gaussian. The significance of the extension is calculated through $TS_{\text{ext}} = 2 \times (\log \mathcal{L}_{\text{ext}} - \log \mathcal{L}_{\text{PS}})$ where \mathcal{L}_{ext} and \mathcal{L}_{PS} are the likelihood obtained with the extended and point-source model, respectively. Since the extended model adds only one parameter to the point-source model (the sigma extent), the significance of the extension is $\sqrt{TS_{\text{ext}}}$. A source is usually considered significantly extended if $TS_{\text{ext}} \geq 16$ (corresponding to 4σ). For 4FGL J0426.5+5434, we found $TS_{\text{ext}} = 7.7$ indicating that the emission is not significantly extended.

We then tested two spatial models to describe the emission of G150.3+4.5: a uniform disk and a 2D symmetric Gaussian. The best-fit position of 4FGL J0426.5+5434 was initially derived with a disk model for G150.3+4.5, following the procedure in the 4FGL catalog. In order to account for possible spatial variations of this point source when using a different spatial model for G150.3+4.5, we fit iteratively (two times) the morphological parameters of G150.3+4.5 (using either the disk or the Gaussian model) and those of 4FGL J0426.5+5434. The best-fit position of 4FGL J0426.5+5434 using the Gaussian model was similar to the one using the disk (with a likelihood variation of 0.2). So we fixed the position of 4FGL J0426.5+5434 to RA_{J2000} = 66.61° and Dec_{J2000} = 54.58° for both spatial models of G150.3+4.5.

Table 1 reports the best-fit positions and extensions obtained for the 2D symmetric Gaussian and disk models, with the associated TS and TS_{ext} values. The Akaike criterion (Akaike 1974) indicates a preference for the 2D symmetric Gaussian model compared to the uniform disk model ($\Delta TS_{\text{Disk} \rightarrow \text{Gaussian}} = 29.2$). A possible source of systematic uncertainties is related to the specific Galactic diffuse model used in the analysis. Thus, we

repeated the analysis using the former diffuse emission models (g11_iem_v06.fits and the associated isotropic component file iso_P8R3_SOURCE_V2.txt). We refit all the sources in the ROI to account for possible spectral differences induced by the different background model before doing the morphological analysis. We still found that the γ -ray emission is best described by a 2D symmetric Gaussian.

We also replaced the extended component by the Urumqi 6 cm map of the SNR (Figure 1, Gao & Han 2014) and we obtained $\Delta TS_{\text{Radio} \rightarrow \text{Gaussian}} = 262.5$ (see Table 1). The residual TS map after fitting the radio template shows significant emission in the inner part of the shell. We therefore tested a two-component model, involving the radio map of the SNR and a 2D symmetric Gaussian, whose best-fit spatial parameters were found to be similar to those listed in Table 1. We found $\Delta TS_{\text{Gaussian} \rightarrow \text{Gaussian} + \text{Radio}} = 1.4$ for three additional parameters, indicating that the radio template does not fit the gamma-ray morphology.

Figure 2 depicts the residual count map and TS map without G150.3+4.5 included in the model with the best-fit spatial models and the radio contours overlaid. The radio emission is spatially coincident with the γ -ray emission, although the brightest parts of the radio and γ -ray emission do not arise from the same region. Residual count maps in different energy bands without G150.3+4.5 and 4FGL J0426.5+5434 included in the model (not shown here) indicate that 4FGL J0426.5+5434 is brighter than G150.3+4.5 below 3 GeV, while the emission from the SNR is dominant at higher energies ($E > 3$ GeV).

We also investigated a possible energy-dependent morphology by fitting a Gaussian and a disk model between 1–10

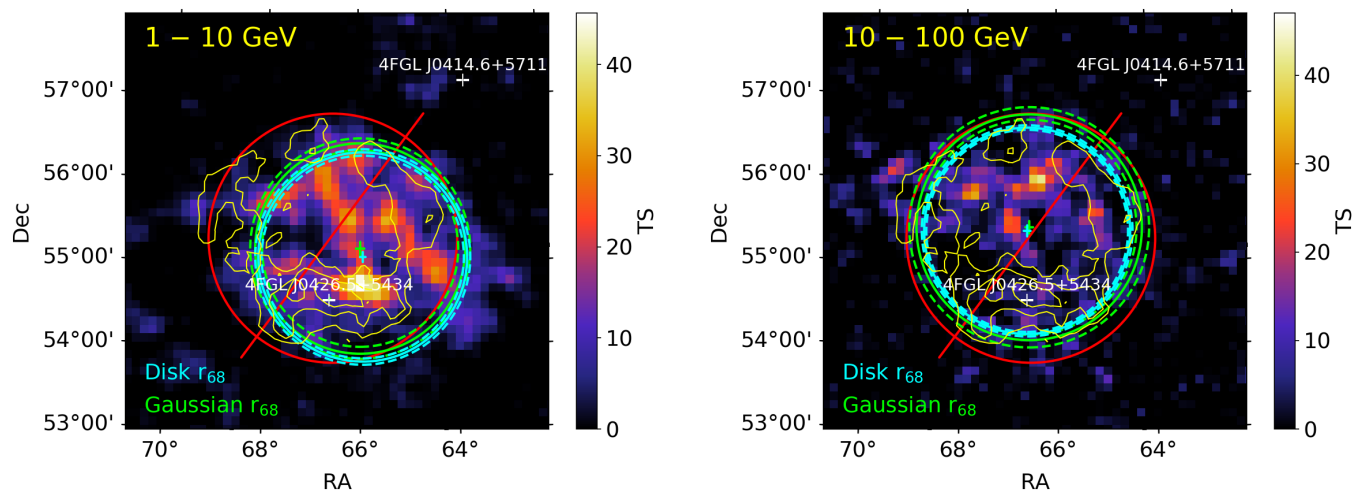


Fig. 3. Residual TS maps without G150.3+4.5 in the model from 1 to 10 GeV (left panel) and 10 to 100 GeV (right panel). The best-fit Gaussian and disk are represented in green and blue, respectively, the crosses being the centroid uncertainties (1σ) and the solid and dashed circles corresponding to the r_{68} with its associated statistical errors (1σ). The white symbols and yellow contours are the same as in Figure 2. The red circle and line show the northeastern and southwestern hemispheres of the best-fit disk found between 1 GeV and 3 TeV (see Section 2.3).

GeV and 10–100 GeV. The comparison between the two spatial models gives $\Delta\text{TS}_{\text{Disk}\rightarrow\text{Gaussian}} = -13.7$ (1–10 GeV) and $\Delta\text{TS}_{\text{Disk}\rightarrow\text{Gaussian}} = 19.5$ (10–100 GeV). Figure 3 shows the residual TS maps without G150.3+4.5 in the model between 1–10 GeV and 10–100 GeV, with the best-fit spatial models overlaid. The low-energy γ -ray emission ($E < 10$ GeV) is dominated by the southwestern part of the SNR, while the centroid of the best-fit spatial models displaces towards the center of the SNR at higher energies ($E > 10$ GeV). We note that the best-fit models from 10 GeV to 100 GeV are very similar to those found between 1 GeV and 3 TeV (Figure 2). The displacement of the centroid of the best-fit models at low energy may be due to a possible contamination from 4FGL J0426.5+5434. Using the Gaussian model, the centroid moves from RA = $65.98^\circ \pm 0.09^\circ$ and Dec = $55.19^\circ \pm 0.08^\circ$ (1–10 GeV) to RA = $66.59^\circ \pm 0.08^\circ$ and Dec = $55.45^\circ \pm 0.08^\circ$ (10–100 GeV). The γ -ray morphology does not shrink at higher energies with the Gaussian extents between 1–10 GeV ($r_{68} = 1.26^{+0.06}_{-0.08}$) and 10–100 GeV ($r_{68} = 1.36^{+0.09}_{-0.06}$) being compatible within statistical errors.

2.3. Spectral analysis

Using the best-fit spatial model found in Section 2.2 (the Gaussian shape for G150.3+4.5), we performed the spectral analysis from 300 MeV to 3 TeV. For comparison, we also performed the same analysis with the disk model. We first fit the spectral parameters of the sources located up to 7° from the ROI center and the normalization of all sources in the model, simultaneously with the Galactic and isotropic diffuse emissions. We verified that no additional sources were needed in the model by examining the residual count and TS maps. When testing different spectral shapes for G150.3+4.5 and 4FGL J0426.5+5434, the spectral parameters of sources located up to 5° from the ROI center were left free during the fit, like those of the Galactic and isotropic diffuse emissions. In the 4FGL catalog, the emission from G150.3+4.5 and 4FGL J0426.5+5434 is described by a LP spectrum of the form

$$\frac{dN}{dE} = N_0 \times \left(\frac{E}{E_0}\right)^{-(\alpha+\beta\log(E/E_0))}. \quad (2)$$

Given our best-fit LP spectral parameters for 4FGL J0426.5+5434, reminiscent of a pulsar, we first replaced its LP spectrum by a power law with an exponential cutoff that did not significantly improve the fit. Keeping the LP to describe the emission of 4FGL J0426.5+5434, we then tried a power-law spectrum for G150.3+4.5 compared to the LP spectrum. We obtained a significant curvature of the spectrum with $\Delta\text{TS}_{\text{PL}\rightarrow\text{LP}} = 23.3$ ($\sim 4.8\sigma$). We also tested a broken power-law spectrum that did not significantly improve the fit compared to the LP spectrum. The spectra of G150.3+4.5 and 4FGL J0426.5+5434 are thus best described with a LP. We repeated the procedure with the model using the disk component and we obtained the same results. The best-fit spectral parameters are listed in Table 2, with the associated statistical and systematic errors. The systematic errors on the spectral analysis depend on our uncertainties on the Galactic diffuse emission model and on the effective area. The former is calculated using eight alternative diffuse emission models following the same procedure as in the first *Fermi*-LAT supernova remnant catalog (Acero et al. 2016) and the latter is obtained by applying two scaling functions on the effective area¹. We also considered the impact on the spectral parameters when changing the spatial model from Gaussian to disk. All these sources of systematic uncertainties (related to the Galactic diffuse emission model, the effective area, and the spatial model) were thus added in quadrature.

The spectrum of G150.3+4.5 is hard, with $\alpha = 1.62 \pm 0.04_{\text{stat}} \pm 0.23_{\text{syst}}$ at $E_0 = 9.0$ GeV, similar to the value obtained for young TeV shell-type SNRs such as RX J1713.7–3946 or RCW 86 (Acero et al. 2015). With a soft spectral index $\alpha = 2.48 \pm 0.08_{\text{stat}} \pm 0.10_{\text{syst}}$ at $E_0 = 651.2$ MeV and a large curvature, 4FGL J0426.5+5434 has a spectrum reminiscent of a pulsar. Barr et al. (2013) found no pulsations from this source with the 100-m Effelsberg radio telescope, making the nature of 4FGL J0426.5+5434 unclear.

Since the centroid of the best-fit spatial models displaces with energy (Section 2.2), we investigated possible spectral differences between the southwestern (SW) and northeastern (NE) parts of the emission, dividing the best-fit disk (found between

¹ https://fermi.gsfc.nasa.gov/ssc/data/analysis/scitools/Aeff_Systematics.html

	N_0 (ph cm $^{-2}$ s $^{-1}$ MeV $^{-1}$)	α	β	E_0 (MeV)	Φ	F
G150.3+4.5- Gaussian	$(7.78 \pm 0.46_{\text{stat}} \pm 1.61_{\text{syst}}) \times 10^{-14}$	$1.62 \pm 0.04_{\text{stat}} \pm 0.22_{\text{syst}}$	$0.07 \pm 0.02_{\text{stat}} \pm 0.02_{\text{syst}}$	8973.8	$6.46^{+10.12}_{-3.54}$	$9.75^{+36.41}_{-5.84}$
4FGL J0426.5+5434	$(1.24 \pm 0.06_{\text{stat}} \pm 0.07_{\text{syst}}) \times 10^{-11}$	$2.48 \pm 0.08_{\text{stat}} \pm 0.10_{\text{syst}}$	$0.41 \pm 0.08_{\text{stat}} \pm 0.11_{\text{syst}}$	651.2	$14.92^{+3.14}_{-2.62}$	$1.52^{+0.52}_{-0.28}$
G150.3+4.5- Disk	$(6.58 \pm 0.40_{\text{stat}} \pm 1.20_{\text{syst}}) \times 10^{-14}$	$1.68 \pm 0.04_{\text{stat}} \pm 0.21_{\text{syst}}$	$0.06 \pm 0.02_{\text{stat}} \pm 0.03_{\text{syst}}$	8973.8	$6.34^{+11.10}_{-3.61}$	$7.95^{+33.88}_{-4.64}$
4FGL J0426.5+5434	$(1.22 \pm 0.06_{\text{stat}} \pm 0.06_{\text{syst}}) \times 10^{-11}$	$2.47 \pm 0.08_{\text{stat}} \pm 0.11_{\text{syst}}$	$0.41 \pm 0.08_{\text{stat}} \pm 0.12_{\text{syst}}$	651.2	$14.70^{+3.06}_{-2.53}$	$1.50^{+0.54}_{-0.28}$

Table 2. Best-fit spectral parameters (from 300 MeV to 3 TeV) with the associated errors obtained for G150.3+4.5 and 4FGL J0426.5+5434 using a logarithmic parabola spectrum, as defined in Equation 2. The first two and last two lines are the parameters obtained when describing the emission from G150.3+4.5 with a Gaussian and a disk respectively. Φ and F are the integral flux and energy flux from 300 MeV to 3 TeV in units of 10^{-9} cm $^{-2}$ s $^{-1}$ and 10^{-11} erg cm $^{-2}$ s $^{-1}$, respectively.

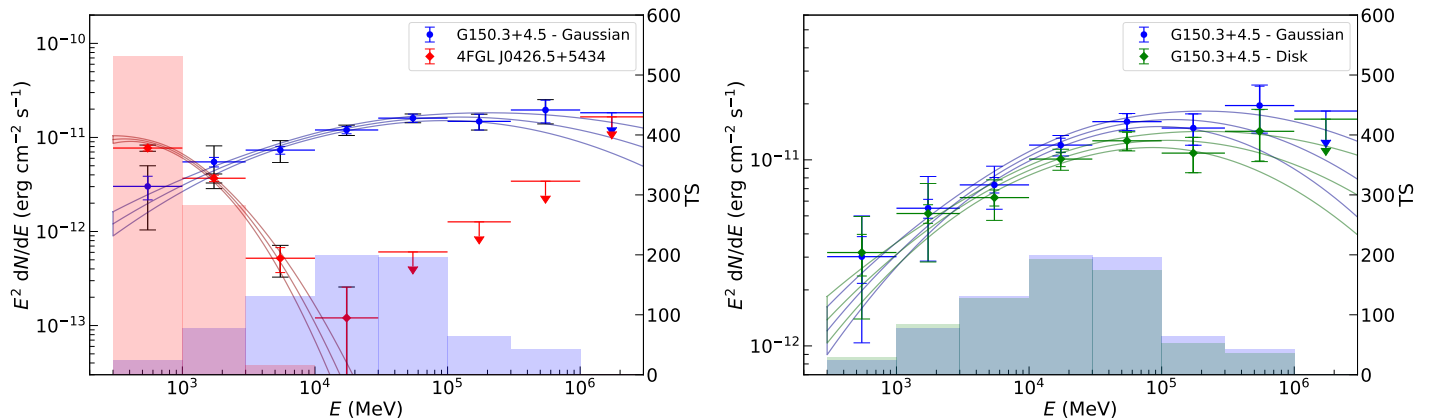


Fig. 4. (Left) SEDs of G150.3+4.5 (blue circles) and 4FGL J0426.5+5434 (red diamonds) with the associated statistical errors (colored bars) and the quadratic sum of the statistical and systematic errors (black bars). The shaded areas correspond to the TS value in each energy band, and the upper limits are calculated at the 95% confidence level. (Right) Comparisons of the SEDs obtained using a Gaussian (blue circles) and a disk (green diamonds) model for G150.3+4.5. For visibility purpose, the colored bars represent the quadratic sum of the statistical and systematic errors.

1 GeV and 3 TeV) into two components (red circle and line in Figure 3). We found a softer spectrum in the SW part than in the NE part, with $\alpha_{\text{NE}} = 1.57 \pm 0.07$ ($\beta_{\text{NE}} = 0.08 \pm 0.03$) and $\alpha_{\text{SW}} = 1.82 \pm 0.06$ ($\beta_{\text{SW}} = 0.04 \pm 0.03$), confirming the morphological analysis in the 1–10 GeV and 10–100 GeV bands. We therefore obtained spectral differences between the NE and SW parts, although both regions exhibit a hard spectrum.

We then computed the spectral energy distributions (SEDs) of the Gaussian and the disk components dividing the whole energy range (300 MeV – 3 TeV) into eight bins. We described the emission of G150.3+4.5 and 4FGL J0426.5+5434 by a power law with fixed spectral index ($\Gamma = 2$) to avoid any dependence on the spectral models. The normalizations of G150.3+4.5 and 4FGL J0426.5+5434 were fit simultaneously with the Galactic and isotropic diffuse emissions (fixing the spectral index of the Galactic component to 0). The normalization of 4FGL J0414.6+5711, located in the northwest of G150.3+4.5 (at $\sim 2.4^\circ$ from the SNR center), was also left free during the fit, while the spectral parameters of the other sources are fixed to their best-fit values found between 300 MeV and 3 TeV since they lie farther than 3.8° from the SNR center. We calculated a flux upper limit in the energy bands where the TS of the source is lower than 1. Figure 4 (left) shows the SEDs of G150.3+4.5 and 4FGL J0426.5+5434, with the statistical and systematic errors. The emission at low energy is dominated by the contribution from 4FGL J0426.5+5434, while the emission from the SNR arises at higher energy. Figure 4 (right) compares the SEDs obtained with the Gaussian and the disk model, showing that the spatial model used for G150.3+4.5 has a negligible impact on the spectral analysis. Since SNRs normally have a sharp edge (and the disk model is found to be spatially coincident with the radio morphology), we use the morphological and spectral prop-

erties of the disk throughout the paper to calculate the physical parameters of the SNR and discuss the nature of the emission.

3. Multiwavelength observations

3.1. H $_I$ spectrum and CO data towards G150.3+4.5

Knowing the distance of G150.3+4.5 is crucial in determining the physical size of the SNR and in turn understanding the origin of the γ -ray emission. Using data from the Leiden/Argentine/Bonn survey of Galactic H $_I$ (Kalberla et al. 2005), we obtained the H $_I$ spectrum in the direction of G150.3+4.5 (shown in Figure 5) that displays clear velocity peaks at -44.7 , -35.9 , -6.9 , and $+2.9$ km s $^{-1}$. The widths of all peaks are 5 km s $^{-1}$ or less, thus there is no evidence of shock-broadening from the SNR shock, where broadening is an indicator of the shock of an SNR overtaking nearby molecular clouds (Wooten 1981). Assuming a flat Galactic rotation curve with Galactocentric distance, $R_0 = 8.34$ kpc, and circular rotation speed at the sun $\Theta = 240$ km s $^{-1}$, the three negative velocities noted above (a positive velocity is not permitted at this Galactic longitude) translate into distances of 4.83, 3.45, and 0.31 kpc, respectively. Since there is no hint of any interaction of the SNR with interstellar material, Figure 5 is only indicative of the H $_I$ emission towards G150.3+4.5 and could be used to derive column density values in future works.

Looking at CO data (Dame et al. 2001), we found molecular contents spatially coincident with the SNR (or at least part of it) with velocities between -9.8 km s $^{-1}$ and -3.8 km s $^{-1}$, which translate into distances of $d = 0.55^{+0.65}_{-0.55}$ kpc and $d = 0.01^{+0.59}_{-0.01}$ kpc, respectively.

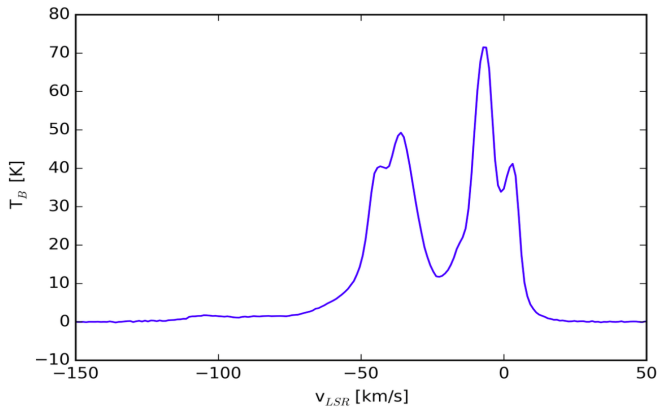


Fig. 5. H I spectrum obtained from the Leiden/Argentine/Bonn survey (Kalberla et al. 2005) in the direction of G150.3+4.5.

3.2. X-ray observations and distance estimate

We used archival observations from the ROSAT all-sky survey (Voges et al. 1999) to determine whether there is significant X-ray emission (0.1–2.4 keV) in the direction of G150.3+4.5. The ROSAT data was extracted within a 1.3° circle centered on RA=4:27:08.528, Dec=+55:27:29.53 with a total exposure of 19 ks (observation ID: WG930708P_N1_SI01.N1, ROSAT/PSPC in survey mode). We used the tool `xselect` to extract the spectrum from the region of interest and the instrument response function (ancillary response function, ARF) was obtained using “`pcarf 2.1.3`”, the latest version of the HEASOFT-FTOOL¹ designed for ROSAT spectrum extraction. The background was derived using an off-source region, excluding any regions that seemed to contain point sources. No significant thermal or non-thermal emission is detected from G150.3+4.5. We modeled the emission using XSPEC² (Arnaud 1996) as an absorbed thermal non-equilibrium ionization (NEI) plasma (Wilms et al. 2000). The Coulomb equilibration timescale is calculated following Vink (2011) and the initial electron temperature is assumed to be the higher of $T_p \times m_e/m_p$ or 0.3 keV (Rakowski et al. 2008). We found a maximum absorbed photon flux of $0.0004 \text{ ph cm}^{-2} \text{ s}^{-1}$ and a corresponding maximum absorbed energy flux of $4.2 \times 10^{-13} \text{ erg cm}^{-2} \text{ s}^{-1}$ between 0.1 and 3.0 keV (with $kT_e = 0.2 \text{ keV}$ and $n_e t = 10^{11} \text{ s cm}^{-3}$). Using a power law with a spectral index $\Gamma = 2$, the maximum absorbed photon and energy fluxes are $0.0005 \text{ ph cm}^{-2} \text{ s}^{-1}$ and $1.1 \times 10^{-12} \text{ erg cm}^{-2} \text{ s}^{-1}$ between 0.1 and 3.0 keV. In the direction of G150.3+4.5, the maximum absorbing column density³ is $N_H = 3.97 \times 10^{21} \text{ cm}^{-2}$, giving maximum unabsorbed thermal and nonthermal photons–energy fluxes of $0.0171 \text{ ph cm}^{-2} \text{ s}^{-1}$ – $8.6 \times 10^{-12} \text{ erg cm}^{-2} \text{ s}^{-1}$ ($kT_e = 0.2 \text{ keV}$, $n_e t = 10^{11} \text{ s cm}^{-3}$) and $0.0063 \text{ ph cm}^{-2} \text{ s}^{-1}$ – $3.6 \times 10^{-12} \text{ erg cm}^{-2} \text{ s}^{-1}$ ($\Gamma = 2$).

To estimate the minimum distance to G150.3+4.5, we used the Sedov-Taylor self-similar solution

$$R_s = \zeta \times \left(\frac{E}{\rho_0} \right)^{1/5} t^{2/5} \quad \text{with} \quad \zeta = 1.152, \quad (3)$$

where R_s , E , ρ_0 , and t are the radius of the SNR, the kinetic energy released by the supernova, the mass ambient density, and

the age of the SNR, respectively. Equation 3 can be written as

$$R_s \approx 0.314 \times \left(\frac{E_{51}}{n_0} \right)^{1/5} t_{\text{yr}}^{2/5} \text{ pc}, \quad (4)$$

where E_{51} is the kinetic energy released by the supernova, n_0 the ambient density, and t_{yr} the age of the SNR in units of $10^{51} \text{ erg cm}^{-3}$, and years. Assuming $E_{51} = 1$ and knowing the angular size of G150.3+4.5, we used different combinations of distance and age to calculate the corresponding ambient density. We then modeled the emission as an absorbed thermal NEI plasma for each combination of age, ambient, and column densities, and electron and proton temperature (Castro et al. 2011). For each distance we thus calculated the corresponding column density, and we obtained an upper limit on the ambient density. The maximum ambient density allowed by ROSAT data is $n_0 = 3.6 \times 10^{-3} \text{ cm}^{-3}$. We also considered that an SNR at a declination of $\sim 55^\circ$ and younger than 1 kyr should have been reported in historical records. Thus, we imposed a lower limit on the age of the SNR of $t = 1 \text{ kyr}$, giving a minimum distance of $d = 0.7 \text{ kpc}$ for an ambient density consistent with ROSAT data ($n_0 = 1.5 \times 10^{-3} \text{ cm}^{-3}$ at that distance). We note that the upper limit on the ambient density is not formally correct since an SNR with $E_{51} = 1$, $M_{\text{ej}} \geq 1.4$ (the ejecta mass in units of solar mass) and $n_0 = 1.5 \times 10^{-3} \text{ cm}^{-3}$ has not yet entered the Sedov phase. This is, however, not critical for deriving an approximate upper limit on the ambient density. For a type Ia SNR, the Sedov phase is reached for $d = 0.9$ – 1 kpc and $t = 3 \text{ kyr}$ ($n_0 \sim 2.3 \times 10^{-3} \text{ cm}^{-3}$).

To constrain the maximum distance, we imposed a Mach number $\mathcal{M}^2 > 10$ (equivalent to a particle spectral index $p < 2.4$). With the sound speed $c_s^2 = \frac{\gamma P_{\text{ISM}}}{\rho_0}$ ($\gamma = 5/3$ being the adiabatic index and P_{ISM} the interstellar medium pressure), this condition can be written as

$$\rho_0 v_s^2 > 10 \rho_0 c_s^2 = 10 \gamma P_{\text{ISM}}. \quad (5)$$

In the Sedov phase, the shock velocity v_s is

$$v_s = \frac{2}{5} \times \frac{R_s}{t}, \quad (6)$$

with R_s and t the shock radius and the age of the SNR, respectively. Using Equation 3, this gives

$$\rho_0 v_s^2 = \left(\frac{2}{5} \right)^2 \zeta^5 \times \frac{E}{R_s^3}. \quad (7)$$

The condition $\rho_0 v_s^2 > 10 \gamma P_{\text{ISM}}$ translates into a relation among the physical radius of the SNR, the interstellar medium pressure, and the kinetic energy released by the supernova

$$R_s < 1.69 \times \left(\frac{P_{\text{ISM}}}{k} \times \frac{1}{E} \right)^{-1/3} \text{ kpc}. \quad (8)$$

Assuming $E_{51} = 1$ and taking $(P_{\text{ISM}}/k) = 2.3 n_0 T_{\text{ISM}} = 3000 \text{ K cm}^{-3}$, we found $R_s < 117.2 \text{ pc}$, giving $d < 4.5 \text{ kpc}$ for $r = 1.497^\circ$. At this distance the age of the SNR is between $t = 161.5 \text{ kyr}$ (using the maximum ambient density $n_0 = 3.6 \times 10^{-3} \text{ cm}^{-3}$ allowed by ROSAT data) and $t = 85.1 \text{ kyr}$ (imposing a lower limit on the ambient density of $n_0 = 1 \times 10^{-3} \text{ cm}^{-3}$).

We note that the assumption $E_{51} = 1$ does not significantly impact the constraint on the ambient density since for $E_{51} = 0.1$ the maximum ambient density allowed by ROSAT data is $n_0 = 3.3 \times 10^{-3} \text{ cm}^{-3}$. The corresponding minimum and maximum distance estimates would be $d = 0.3 \text{ kpc}$ and $d = 2.1 \text{ kpc}$.

In the following sections we assume $E_{51} = 1$, and we use the minimum and maximum distance estimate $d = 0.7 \text{ kpc}$ ($t = 1 \text{ kyr}$, $R_s = 18.3 \text{ pc}$, $n_0 = 1.5 \times 10^{-3} \text{ cm}^{-3}$) and $d = 4.5 \text{ kpc}$ ($t = 85.1$ – 161.5 kyr , $R_s = 117.2 \text{ pc}$, $n_0 = (1.0$ – $3.6) \times 10^{-3} \text{ cm}^{-3}$) to discuss the origin of the emission.

¹ <http://heasarc.gsfc.nasa.gov/ftools>

² <https://heasarc.gsfc.nasa.gov/xanadu/xspec/>

³ Calculated with the Chandra Proposal Planning Toolkit <https://cxc.harvard.edu/toolkit/colden.jsp>

4. Discussion

4.1. Supernova remnant or pulsar wind nebula?

The γ -ray data analysis presented here has led to the characterization of an extended γ -ray source whose centroid and extent are spatially coincident with the radio SNR. The broad size of the extended source and the correlation with the radio shell leaves few plausible scenarios for the nature of the γ -ray emission. Namely, the GeV emission can either arise from a pulsar wind nebula (PWN) or from an SNR.

The Gaussian morphology of the γ -ray emission and the hard γ -ray spectral index extending to hundreds of GeV make plausible the PWN scenario. However, the γ -ray morphology does not get smaller at higher energies (Figure 3) as expected from electron cooling, and ROSAT X-ray observations detect no significant nonthermal emission suggestive of a PWN in the direction of G150.3+4.5 (Section 3.2). We nevertheless note that if the source is located at a large distance, the absorption of low-energy X-ray photons can prevent such a detection. The radio spectral index of the eastern shell ($\alpha = -0.62 \pm 0.07$ and $\alpha = -0.40 \pm 0.17$, Gerbrandt et al. 2014; Gao & Han 2014) and of the western shell ($\alpha = -0.69 \pm 0.24$, Gao & Han 2014), both spatially coincident with the γ -ray extent, are more compatible with that obtained for SNRs than for PWNe. Typical PWN radio spectral indices range from about $-0.3 \lesssim \alpha \lesssim 0$, while SNRs usually have a steeper radio spectral index $\alpha \lesssim -0.4$ (Green 2017). Thus, the measured radio spectral index disfavors a PWN scenario as the origin of the emission. Furthermore, there is no pulsar in the vicinity of the γ -ray emission that could power a PWN. The source 4FGL J0426.5+5434, located in the southern part of the SNR, has a pulsar-like spectrum and no pulsations were found with the 100-m Effelsberg radio telescope (Barr et al. 2013). However, this potential pulsar could be radio quiet, or intensity variations from interstellar scintillation could have prevented detection at the epoch of observation. Therefore 4FGL J0426.5+5434 may be a pulsar or another background source. Assuming that 4FGL J0426.5+5434 was the compact remnant of the progenitor star that birthed G150.3+4.5, with an angular distance from the radio SNR center of 0.881° , it would have to be traveling with a velocity of $v_{\text{PSR}} \sim 10533 \text{ km s}^{-1}$ (taking $d = 0.7 \text{ kpc}$ and $t = 1 \text{ kyr}$) or $v_{\text{PSR}} \sim 419\text{--}796 \text{ km s}^{-1}$ (taking $d = 4.5 \text{ kpc}$ and $t = 161.5\text{--}85.1 \text{ kyr}$). Typical pulsar velocities range from $v_{\text{PSR}} \sim 400\text{--}500 \text{ km s}^{-1}$ (Lyne & Lorimer 1995), with extreme velocities exceeding 1000 km s^{-1} (Chatterjee et al. 2005). Thus, the association between G150.3+4.5 and 4FGL J0426.5+5434 would only be possible when considering relatively far distances, such as $d = 4.5 \text{ kpc}$. From the spectral properties of 4FGL J0426.5+5434 reported in Table 2, we calculated an energy flux of $F_{0.1\text{--}100 \text{ GeV}} = 2.31 \times 10^{-11} \text{ erg cm}^{-2} \text{ s}^{-1}$, giving a luminosity $L_{0.1\text{--}100 \text{ GeV}} = 5.60 \times 10^{34} (d/4.5 \text{ kpc})^2 \text{ erg s}^{-1}$. The empirical relation between the luminosity and the spin-down power of the pulsar $L_{0.1\text{--}100 \text{ GeV}} = \sqrt{10^{33} \dot{E}} \text{ erg s}^{-1}$ (Abdo et al. 2013) gives $\dot{E} = 3.14 \times 10^{36} (d/4.5 \text{ kpc})^4 \text{ erg s}^{-1}$ (taking a beam correction factor of 1), indicating that 4FGL J0426.5+5434 could be an energetic pulsar. However, if 4FGL J0426.5+5434 is associated with the SNR and powers a PWN responsible for the observed GeV emission, the PWN γ -ray extent would be as large as the radio extent of its host SNR which never occurs in composite systems. All these arguments disfavor a PWN scenario as the origin of the main γ -ray emission, keeping in mind that a PWN located in the line of sight and contributing to a part of the γ -ray emission cannot be ruled out.

The spatial correlation between the radio and the γ -ray emissions, together with the lack of a γ -ray morphology shrinking at higher energies, points toward an SNR scenario. This is supported by the radio shell-like appearance, the nonthermal radio spectrum similar to that obtained in SNRs, and the detection of red optical filaments structures by Gerbrandt et al. (2014). Unless a pulsar is detected in the future that could power a PWN contributing to the GeV emission, we argue that the γ -ray emission is likely produced by the SNR G150.3+4.5 and is the counterpart of the radio emission detected by Gao & Han (2014).

4.2. Evolutionary stage of G150.3+4.5

In the following sections we assume that the entire γ -ray emission comes from the SNR G150.3+4.5. We place the SNR in context within the current population of *Fermi*-LAT SNRs to assess its evolutionary stage. Figure 6 shows the *Fermi*-LAT SED of G150.3+4.5 (obtained in Section 2.3 using a uniform disk) overlaid on the spectra of several *Fermi*-LAT observed SNRs with ages ranging from ~ 1 to 20 kyr. As shown in Figure 6, spectral breaks are commonly observed below a few GeV in SNRs interacting with nearby molecular material. G150.3+4.5 exhibits a hard spectrum extending to hundreds of GeV with no spectral break, and is thus spectrally similar to the dynamically young and shell-type SNRs like RX J1713.7–3946 or Vela Junior.

Figure 7 depicts the luminosity of several *Fermi*-LAT SNRs with respect to their diameter squared. Between 100 MeV to 100 GeV, G150.3+4.5 has a luminosity of $2.53 \times 10^{33} (d/0.7 \text{ kpc})^2 \text{ erg s}^{-1}$. For the minimum distance, the luminosity of G150.3+4.5 is low and similar to that obtained for young SNRs, while for the maximum distance the luminosity is closer to those of SNRs interacting with molecular clouds (MCs). However, there is no hint of an interaction between G150.3+4.5 and a MC in the radio data explored by Gerbrandt et al. (2014) and Gao & Han (2014), as in the catalog of molecular clouds (Rice et al. 2016) and of Galactic H II regions (Anderson et al. 2014), which do not report any object close to G150.3+4.5. The hard spectral shape of G150.3+4.5 and its likely low luminosity from 100 MeV to 100 GeV supports the dynamically young and non-interacting SNR scenario, and therefore a near distance.

4.3. Broadband nonthermal modeling

Particle acceleration arises at the shock front of the SNR G150.3+4.5, producing γ rays up to hundreds of GeV. These γ rays can either be produced by accelerated electrons through IC scattering on photon fields and Bremsstrahlung, or by accelerated protons colliding with ambient matter and leading to the decay of the neutral pion. To understand the origin of the emission, we performed multiwavelength modeling using the *naïma* package (Zabalza 2015) in a one-zone model assumption. As shown in Figure 4 (right), the choice of the spatial model for G150.3+4.5 has no impact on the spectral analysis. We used the radio fluxes derived in Gerbrandt et al. (2014) and the γ -ray spectrum obtained with the disk model (Section 2.2), and we factored the X-ray absorption into the model, allowing the use of the robust upper limit on the absorbed X-ray flux obtained with ROSAT data (Section 3.2). Since the radio fluxes were derived in a region of $\sim 2.14^\circ \times 0.63^\circ$ (Gerbrandt et al. 2014) that does not encompass the entire radio SNR ($\sim 3^\circ \times 2^\circ$, as reported in Gao & Han 2014), we considered these data points as lower limits. We modeled the broadband nonthermal emission of the SNR

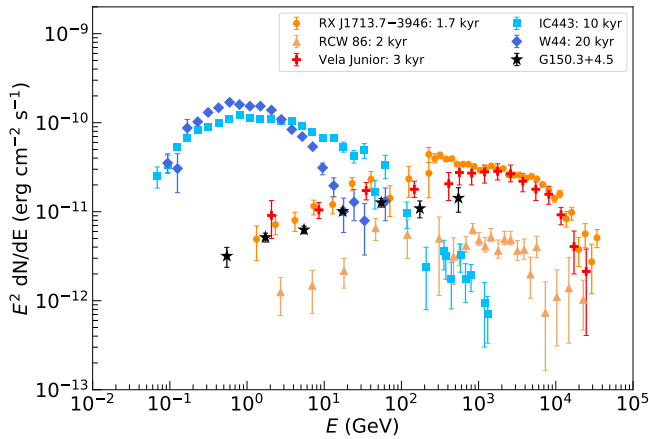


Fig. 6. SEDs of several *Fermi*-LAT SNRs interacting with molecular clouds (blue tone colors) and being dynamically young (orange tone colors). The black stars correspond to the SED of G150.3+4.5 shown in Figure 4 (right) using the disk model. References: RX J1713.7–3946 (H. E. S. S. Collaboration et al. 2018a), RCW 86 (Ajello et al. 2016), Vela Junior (H. E. S. S. Collaboration et al. 2018b), IC 443, and W44 (Ackermann et al. 2013).

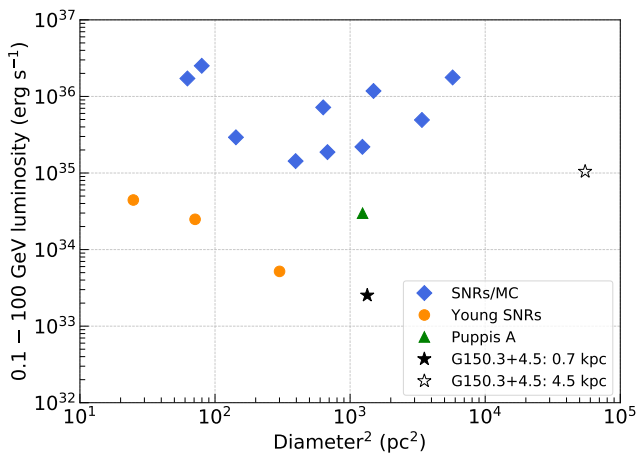


Fig. 7. Luminosity (0.1–100 GeV) of several *Fermi*-LAT observed SNRs plotted against their diameter squared. Blue diamonds are the SNRs interacting with molecular clouds, while orange circles are young SNRs. The SNR Puppis A, a middle-aged SNR that is not interacting with a molecular cloud, is represented by the green triangle. Black stars correspond to the SNR G150.3+4.5 using a distance of 0.7 kpc and 4.5 kpc, respectively. The figure is reproduced from Thompson et al. (2012) with the addition of G150.3+4.5.

assuming $E_{51} = 1$ and for the two extreme distances $d = 0.7$ kpc and $d = 4.5$ kpc.

We described the proton spectrum by a power law with an exponential cutoff (defining the maximum energy reached by the particles) and the electron spectrum by a broken power law with an exponential cutoff. The break in the electron spectrum is due to synchrotron cooling, and occurs at the energy E_b above which the particle spectral index is $s_{e,2} = s_{e,1} + 1$, with $s_{e,1}$ being the spectral index below the energy break. To be consistent with the measured radio spectral index ($\alpha = -0.38 \pm 0.10$), we fixed the electron spectral index to $s_{e,1} = 1.8$, giving $s_{e,2} = 2.8$, and we used the same value for the proton spectral index $s_p = 1.8$. To constrain the energy break and the particle maximum energy, we considered the synchrotron loss time

$$\tau_{\text{sync}} = (1.25 \times 10^3) \times E_{\text{TeV}}^{-1} B_{100}^{-2} \text{ yr} \quad (9)$$

and the acceleration timescale

$$t_{\text{acc}} = 30.6 \times \frac{3r^2}{16(r-1)} \times k_0(E) \times E_{\text{TeV}} B_{100}^{-1} v_{s,3}^{-2} \text{ yr}, \quad (10)$$

where r is the shock compression ratio, k_0 is the ratio between the mean free path and the gyroradius (equivalent to $B_{\text{tot}}^2 / B_{\text{turb}}^2$), and B_{100} and $v_{s,3}$ are the magnetic field and the shock velocity in units of 100 μG and 1000 km s^{-1} , respectively (Pari-zot et al. 2006). For young SNRs we expect $k_0 \sim 1$, while for evolved systems we expect $k_0 > 1$. The break and maximum energy of the electrons are calculated equating $\tau_{\text{sync}} = t_{\text{age}}$ and $t_{\text{acc}} = \min(t_{\text{age}}, \tau_{\text{sync}})$, respectively, while the maximum energy of the protons is found with $t_{\text{age}} = t_{\text{acc}}$. For the IC scattering on photon fields, we considered the cosmic microwave background ($U_{\text{CMB}} = 0.26 \text{ eV cm}^{-3}$, $T_{\text{CMB}} = 2.7 \text{ K}$), the infrared and optical emissions for which the temperature and energy density are estimated with the GALPROP code¹ (Porter et al. 2008). The total energy of accelerated particles is integrated above 1 GeV.

For a distance of $d = 0.7$ kpc, the temperature and energy density of the infrared and optical emissions are $T_{\text{IR}} = 25.2 \text{ K}$, $U_{\text{IR}} = 0.34 \text{ eV cm}^{-3}$ and $T_{\text{opt}} = 2004.9 \text{ K}$, $U_{\text{opt}} = 0.52 \text{ eV cm}^{-3}$. We used the ambient density of $n_0 = 1.5 \times 10^{-3} \text{ cm}^{-3}$ derived in Section 3.2, and the column density of $N_H = 5.23 \times 10^{20} \text{ cm}^{-2}$ (corresponding to a distance of $d = 0.7$ kpc) to model the absorbed X-ray nonthermal emission. The radio fluxes constrain the magnetic field to be relatively low. With $W_p = 10^{50} \text{ erg}$ (10% of E_{51} going into CR protons), the data can be reproduced with a downstream magnetic field of $B = 5 \mu\text{G}$ and an electron-to-proton ratio of $K_{\text{ep}} = 1 \times 10^{-3}$. We used the value of the velocity in the Sedov phase $v_s = 7163 \text{ km s}^{-1}$, which is consistent with the data for $E_b = E_{\text{max,e}} = E_{\text{max,p}} = 5.2 \text{ TeV}$ implying $k_0 = 16$ (using $r = 4$). Given the low magnetic field and age of the SNR, electrons do not suffer significantly from synchrotron cooling so there is no break in the electron spectrum. We note that if the SNR is in the ejecta-dominated phase, the velocity should be even higher than $v_s = 7163 \text{ km s}^{-1}$. Although the value of k_0 is unknown, $k_0 = 16$ is higher than one would expect. Since we have $E_{\text{max}} \propto v_s^2 / k_0$, a lower value of k_0 would imply a reduced shock velocity to still fit the data. That could indicate that the SNR is located at a larger distance than 0.7 kpc (since we have $v_s \propto R_s^{-3}$). Table 3 reports the physical parameters used for the broadband modeling of the SNR spectrum, shown in Figure 8 (left).

For a distance of $d = 4.5$ kpc, the temperature and the energy density of the infrared and optical emissions are $T_{\text{IR}} = 25.2 \text{ K}$, $U_{\text{IR}} = 0.11 \text{ eV cm}^{-3}$ and $T_{\text{opt}} = 2004.9 \text{ K}$, $U_{\text{opt}} = 0.24 \text{ eV cm}^{-3}$. We first discuss the case of $t = 85.1 \text{ kyr}$ obtained with $n_0 = 1.0 \times 10^{-3} \text{ cm}^{-3}$ and we used a column density of $N_H = 2.63 \times 10^{21} \text{ cm}^{-2}$ for the absorbed X-ray synchrotron model (corresponding to $d = 4.5$ kpc). Setting $W_p = 10^{50} \text{ erg}$ and using a shock velocity of $v_s = 539 \text{ km s}^{-1}$ calculated in the Sedov model, the data can be reproduced with $B = 5 \mu\text{G}$, $K_{\text{ep}} = 5 \times 10^{-2}$, and $E_b = E_{\text{max,e}} = E_{\text{max,p}} = 5.8 \text{ TeV}$ obtained using $k_0 = 7$. The spectrum is shown in Figure 8 (right) with the corresponding values reported in Table 3. For $t = 161.5 \text{ kyr}$, the shock velocity in the Sedov phase is $v_s = 284 \text{ km s}^{-1}$ implying a lower value of k_0 to still fit the data. We also note that the value of $K_{\text{ep}} = 5 \times 10^{-2}$ is slightly higher than one would expect, strengthening the fact that the distance of G150.3+4.5 is likely smaller than $d = 4.5$ kpc.

Using the two extreme distances of $d = 0.7$ kpc and $d = 4.5$ kpc, the broadband spectrum of the SNR is explained by a leptonic scenario, with acceleration of particles up to $\sim 5 \text{ TeV}$ and

¹ <https://galprop.stanford.edu>

d (kpc) / t (kyr)	B (μG)	W_p (erg)	K_{ep}	$s_{e,1} = s_{e,2}$	s_p	n_0 (cm^{-3})	$E_{\text{max},e}$ (TeV)	$E_{\text{max},p}$ (TeV)	k_0	v_s (km s^{-1})
0.7 / 1.0	5	10^{50}	1×10^{-3}	1.8*	1.8	1.5×10^{-3}	5.2	5.2	16	7163
4.5 / 85.1	5	10^{50}	5×10^{-2}	1.8*	1.8	1.0×10^{-3}	5.8	5.8	7	539

Table 3. Values used for the broadband nonthermal modeling shown in Figure 8. Asterisks denote the values constrained by radio data. The particle maximum energy values ($E_{\text{max},e}$ and $E_{\text{max},p}$) are calculated using the values of B , k_0 , and the shock velocity v_s derived in the Sedov model.

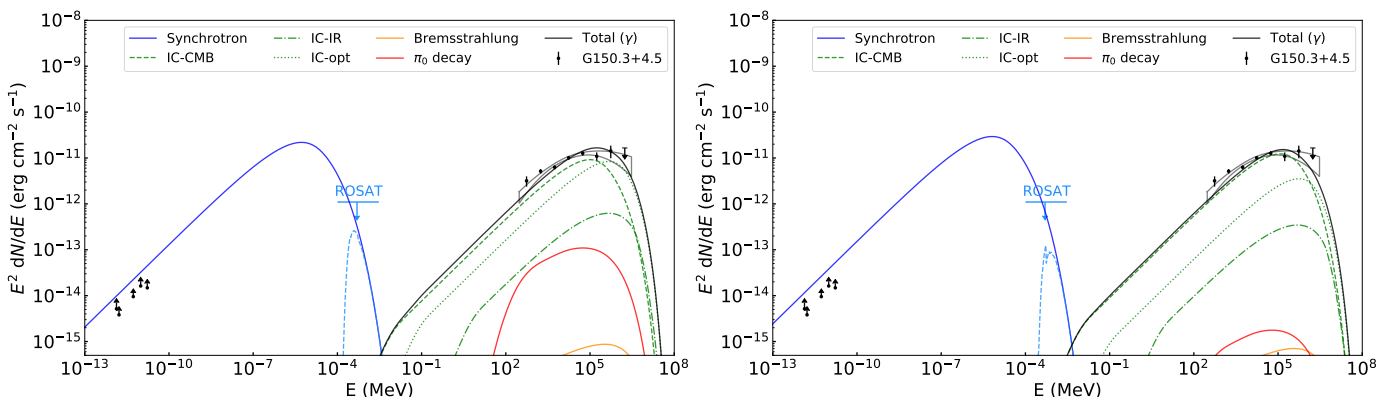


Fig. 8. Broadband nonthermal modeling of the SNR G150.3+4.5 in a leptonic scenario using a distance of $d = 0.7$ kpc (left) and $d = 4.5$ kpc (right). The radio fluxes, which are near lower limits (see Section 4.3), come from Gerbrandt et al. (2014) and the best-fit spectrum and γ -ray fluxes are those derived using the disk model. The ROSAT upper limit on the absorbed flux is derived in Section 3.2 and has to be compared to the absorbed X-ray synchrotron model (dashed blue curve). The values used for the plots are reported in Table 3.

a downstream magnetic field of $B = 5 \mu\text{G}$. Under standard shock conditions, this gives an interstellar magnetic field of $B_{\text{ISM}} = 1.5 \mu\text{G}$ (taking the isotropic compression ratio with $r = 4$). Since the radio fluxes derived in Gerbrandt et al. (2014) are likely underestimated, we used them as near lower limits. In each of our models, the synchrotron flux never exceeds ~ 2 – 3 times the values of the radio data, which is reasonable given the difference between the extraction region size taken in Gerbrandt et al. (2014) and the extent of the radio SNR (assuming a uniform emission). The minimum and maximum distances respectively require a higher value of k_0 and K_{ep} than one would expect, which indicate that the SNR is indeed located between 0.7 kpc and 4.5 kpc. We did not consider the hadron-dominated scenario due to the low maximum ambient density allowed by ROSAT data (Section 3.2), which would lead to an unrealistic value of W_p , and due to the lack of any hint of interaction of the SNR with interstellar material (Section 3.1). For the same reason, we also note that the SNR is likely not located at the same distance as those of the enhanced H I and CO emissions (derived in Section 3.1).

Deeper multiwavelength observations are necessary to better constrain the broadband emission from G150.3+4.5. That concerns radio observations to derive the synchrotron spectrum in a region encompassing the entire SNR, X-ray observations to obtain stronger upper limits on the thermal emission and very high-energy observations with Cherenkov telescopes to assess the maximum energy reached by particles in this Galactic cosmic-ray accelerator. Finally, a distance estimate would allow us to more precisely determine the evolutionary stage of the SNR G150.3+4.5.

5. Conclusions

We analyzed more than 10 years of *Fermi*-LAT data and we investigated the morphological and the spectral properties of the γ -ray emission towards the recently detected radio SNR G150.3+4.5. From 1 GeV to 3 TeV the emission is adequately described by a 2D symmetric Gaussian or a disk model, which is spatially coincident with the radio emission. Going down to 300

MeV, the spectrum is best described by a logarithmic parabola with a hard spectral index $\alpha = 1.62 \pm 0.04_{\text{stat}} \pm 0.23_{\text{sys}}$ at $E_0 = 9.0$ GeV. The point source 4FGL J0426.5+5434, located in the southern part of the SNR, has a pulsar-like spectrum and dominates the low-energy part of the γ -ray emission ($E < 3$ GeV), while the contribution from the SNR arises at higher energy.

We did not detect significant thermal and nonthermal X-ray emission using ROSAT all-sky survey data, which implies a maximum ambient density $n_0 = 3.6 \times 10^{-3} \text{ cm}^{-3}$. Setting a lower limit on the age of the SNR $t = 1$ kyr, we estimated a minimum distance of $d = 0.7$ kpc, which is consistent with the ROSAT upper limit on the ambient density. Using physical considerations, we estimated a maximum distance of $d = 4.5$ kpc. Using the maximum ambient density allowed by ROSAT data and a lower limit of $n_0 = 0.1 \times 10^{-3}$, the age of the SNR is $t = 85.1$ – 161.5 kyr.

The association between G150.3+4.5 and the pulsar-like 4FGL J0426.5+5434 is unclear and would be possible only if the SNR is located at relatively far distances, giving 4FGL J0426.5+5434 a reasonable transverse velocity. Since there is no hint for a PWN as the origin of the γ -ray emission, the latter being spatially coincident with the radio SNR, we argued that the GeV emission is likely produced by the SNR G150.3+4.5. We compared the spectrum and luminosity of G150.3+4.5 with those of other *Fermi*-LAT observed SNRs, including young systems and evolved SNRs interacting with molecular clouds. We found that G150.3+4.5 is spectrally similar to the dynamically young and shell-type *Fermi*-LAT SNRs. We modeled the broadband nonthermal emission of G150.3+4.5 with a leptonic scenario that implies a downstream magnetic field of $B = 5 \mu\text{G}$ and an acceleration of particles up to few TeV energies.

Deeper multiwavelength observations are required to better constrain the distance, the environment of G150.3+4.5 and its synchrotron spectrum. Since the detection of X-ray emission with *Chandra* or *XMM-Newton* can be challenging for sources with an angular size of 3° , large field-of-view X-ray instruments like eROSITA would be helpful to assess any thermal and non-

thermal emission towards G150.3+4.5. Very high-energy analyses are promising in constraining the highest part of the γ -ray spectrum. Although not detected with 507 days of observations by HAWC (Abeyssekara et al. 2017), G150.3+4.5 is a good candidate to be observed with the next generation of Cherenkov telescopes CTA (Cherenkov Telescope Array) that will give clear insights into the maximum energy reached by particles in this dynamically young SNR. Finally, deeper pulsation searches on 4FGL J0426.5+5434 would help investigate its nature and its possible association with G150.3+4.5.

Acknowledgements. We thank the referee for the helpful comments on this paper, and X. Y. Gao and J. L. Han for providing us the Urumqi 6 cm map of the SNR. JD, MLG and MHG acknowledge support from Agence Nationale de la Recherche (grant ANR-17-CE31-0014). The Fermi LAT Collaboration acknowledges generous ongoing support from a number of agencies and institutes that have supported both the development and the operation of the LAT as well as scientific data analysis. These include the National Aeronautics and Space Administration and the Department of Energy in the United States, the Commissariat à l’Énergie Atomique and the Centre National de la Recherche Scientifique / Institut National de Physique Nucléaire et de Physique des Particules in France, the Agenzia Spaziale Italiana and the Istituto Nazionale di Fisica Nucleare in Italy, the Ministry of Education, Culture, Sports, Science and Technology (MEXT), High Energy Accelerator Research Organization (KEK) and Japan Aerospace Exploration Agency (JAXA) in Japan, and the K. A. Wallenberg Foundation, the Swedish Research Council and the Swedish National Space Board in Sweden. Additional support for science analysis during the operations phase is gratefully acknowledged from the Istituto Nazionale di Astrofisica in Italy and the Centre National d’Études Spatiales in France. This work performed in part under DOE Contract DE-AC02-76SF00515.

References

- Abdo, A. A., Ajello, M., Allafort, A., et al. 2013, *ApJS*, 208, 17
- Abeyssekara, A. U., Albert, A., Alfaro, R., et al. 2017, *ApJ*, 843, 40
- Abeyssekara, A. U., Archer, A., Benbow, W., et al. 2020, *ApJ*, 894, 51
- Acero, F., Ackermann, M., Ajello, M., et al. 2016, *ApJS*, 224, 8
- Acero, F., Lemoine-Goumard, M., Renaud, M., et al. 2015, *A&A*, 580, A74
- Ackermann, M., Ajello, M., Allafort, A., et al. 2013, *Science*, 339, 807
- Ackermann, M., Ajello, M., Atwood, W. B., et al. 2016, *ApJS*, 222, 5
- Ackermann, M., Ajello, M., Baldini, L., et al. 2017, *ApJ*, 843, 139
- Ahnen, M. L., Ansoldi, S., Antonelli, L. A., et al. 2017, *MNRAS*, 472, 2956
- Ajello, M., Baldini, L., Barbiellini, G., et al. 2016, *ApJ*, 819, 98
- Akaike, H. 1974, *IEEE Transactions on Automatic Control*, 19, 716
- Anderson, L. D., Bania, T. M., Balsler, D. S., et al. 2014, *ApJS*, 212, 1
- Arnaud, K. A. 1996, *Astronomical Society of the Pacific Conference Series*, Vol. 101, *XSPEC: The First Ten Years*, ed. G. H. Jacoby & J. Barnes, 17
- Atwood, W. B., Abdo, A. A., Ackermann, M., et al. 2009, *ApJ*, 697, 1071
- Barr, E. D., Guillemot, L., Champion, D. J., et al. 2013, *MNRAS*, 429, 1633
- Bell, A. R. 1978, *MNRAS*, 182, 147
- Castro, D., Slane, P., Patnaude, D. J., & Ellison, D. C. 2011, *The Astrophysical Journal*, 734, 85
- Chatterjee, S., Vlemmings, W. H. T., Brisken, W. F., et al. 2005, *ApJ*, 630, L61
- Dame, T. M., Hartmann, D., & Thaddeus, P. 2001, *ApJ*, 547, 792
- Gao, X. Y. & Han, J. L. 2014, *A&A*, 567, A59
- Gerbrandt, S., Foster, T. J., Kothes, R., Geisbüsch, J., & Tung, A. 2014, *A&A*, 566, A76
- Green, D. A. 2017, *VizieR Online Data Catalog*, VII/278
- H. E. S. S. Collaboration, Abdalla, H., Abramowski, A., et al. 2018a, *A&A*, 612, A6
- H. E. S. S. Collaboration, Abdalla, H., Abramowski, A., et al. 2018b, *A&A*, 612, A7
- Kalberla, P. M. W., Burton, W. B., Hartmann, D., et al. 2005, *A&A*, 440, 775
- Lyne, A. G. & Lorimer, D. R. 1995, *Journal of Astrophysics and Astronomy*, 16, 97
- Parizot, E., Marcowith, A., Ballet, J., & Gallant, Y. A. 2006, *A&A*, 453, 387
- Porter, T. A., Moskalenko, I. V., Strong, A. W., Orlando, E., & Bouchet, L. 2008, *ApJ*, 682, 400
- Rakowski, C. E., Laming, J. M., & Ghavamian, P. 2008, *The Astrophysical Journal*, 684, 348
- Rice, T. S., Goodman, A. A., Bergin, E. A., Beaumont, C., & Dame, T. M. 2016, *ApJ*, 822, 52
- The Fermi-LAT collaboration. 2019, *arXiv e-prints*, arXiv:1902.10045
- Thompson, D. J., Baldini, L., & Uchiyama, Y. 2012, *Astroparticle Physics*, 39, 22
- Vink, J. 2011, *The Astronomy and Astrophysics Review*, 20, 49
- Voges, W., Aschenbach, B., Boller, T., et al. 1999, *VizieR Online Data Catalog*, 9010
- Wilms, J., Allen, A., & McCray, R. 2000, *The Astrophysical Journal*, 542, 914
- Wood, M., Caputo, R., Charles, E., et al. 2017, *International Cosmic Ray Conference*, 301, 824
- Wooten, A. 1981, *ApJ*, 245, 105
- Yuan, Y., Funk, S., Jóhannesson, G., et al. 2013, *ApJ*, 779, 117
- Zabalza, V. 2015, in *34th International Cosmic Ray Conference (ICRC2015)*, Vol. 34, 922